



# Study of the Photocatalytic Activity Using Silica-Based Materials Doped with Silver Nanoparticles for Degradation of Rhodamine B Dye

Lázaro Nascimento Ribas · Luis Otávio de Sousa Bulhões · William Leonardo da Silva

Received: 13 February 2020 / Accepted: 26 March 2020 / Published online: 18 April 2020  
© Springer Nature Switzerland AG 2020

**Abstract** Rhodamine B (RhB) is a cationic organic dye widely used industrially, mainly in the textile and food industries. Then, the work aims to study on the photocatalytic degradation of RhB dye, under UV and visible radiation, using photocatalyst silica-based materials synthesized by sol-gel route with different solvents (ethanol and n-propanol) and catalysts ( $C_{12}H_{27}N$ ,  $HNO_3$ ,  $NH_4OH$ , and  $NaOH$ ) to the hydrolysis and condensation of tetraorthosilicate (TEOS). In addition, the effect of doping with silver nanoparticles (AgNPs) was evaluated on the photocatalytic activity. The samples were characterized by X-ray diffraction (XRD), diffuse reflectance spectroscopy (DRS),  $N_2$  porosimetry, zeta potential measurements (ZP), and Fourier transform infrared spectroscopy (FTIR). To evaluate the photocatalytic activity, photocatalytic tests were carried out in a stirred batch reactor, with the photocatalyst in suspension, under ultraviolet and visible radiation, and the target molecule chosen was the Rhodamine B dye (RhB). The photocatalyst Si-HNO<sub>3</sub>-AgNPs showed the best photocatalytic activity with a degradation of the RhB dye of 90.16% ( $k = 0.0198 \text{ min}^{-1}$ , under ultraviolet radiation) and 82.79% ( $k = 0.0148 \text{ min}^{-1}$ , under visible radiation), after 120 min of reaction; while under

the same conditions, the commercial catalyst  $TiO_2$  (P25) showed a degradation of 50.02% and 42.14%, respectively.

**Keywords** Heterogeneous photocatalysis · Doping · Silver nanoparticles · Dyes · Sol-gel

## 1 Introduction

Currently, problems related to supply and wastewater pollution are potentially caused due to the presence of organic pollutants, mainly dyes and pharmaceuticals (Lu et al. 2019). Furthermore, the presence of dyes in wastewater becomes associated with being in textile, food, and plastic industries as main sources spending a lot of volume of water, producing remarkable color wastewater (Rafatullah et al. 2010). For example, it is estimated that there are more than 100,000 synthetic dyes on the market, with the annual production more of 700,000 tons around the world (Al-Fawwaz and Abdullah 2015). Thus, the fact is that many of these compounds are characterized by toxic nature and their proprieties mutagenic and carcinogenic, becoming a threat to public health and the environment (Kassale et al. 2015). Among these dyes, Rhodamine B ( $C_{28}H_{31}N_2O_3Cl$ ) is characterized by its cationic nature, belonging to the class of xanthenic dyes and widely used in the textile industry and as a tracing material, presenting high solubility in water and organic solvent (Rajkumar and Kim 2006). In addition, it is potentially harmful to humans as it may promote skin, eye, and

L. Nascimento Ribas · W. L. da Silva  
Chemical Engineering Course, Franciscan University, Santa Maria, RS 97010-032, Brazil

L. O. de Sousa Bulhões · W. L. da Silva (✉)  
Postgraduate Program in Nanosciences, Franciscan University, Santa Maria, RS 97010-032, Brazil  
e-mail: w.silva@ufn.edu.br

respiratory system irritation (Cheng et al. 2017). Figure 1 shows the molecular structure of the RhB dye, where it is possible to verify the presence of chromophoric groups ( $-C=C-/-C=N-$ ), which gives the pink color, a characteristic of RhB.

Thus, the treatment of wastewater containing RhB becomes essential for environmental protection. In this way, several techniques for its degradation and mineralization have been investigated, such as adsorption (Zhang et al. 2012) and advanced oxidative processes (AOPs) (Gao et al. 2015; Patil et al. 2016). Advanced oxidative processes (AOPs) become an attractive alternative as they are technologies with the potential to oxidize a wide variety of complex organic compounds (Ma et al. 2014) through the action of a highly oxidizing species (hydroxyl radical  $\bullet OH$ ), able to react with various resistant organic compounds, mineralizing them in non-toxic forms, such as  $CO_2$  and  $H_2O$  (Wu et al. 2016). Among the AOPs, heterogeneous photocatalysis stands out, since it is a process that involves radiation-induced redox reactions on the surface of semiconductors (photocatalysts), such as titanium dioxide ( $TiO_2$ ) and zinc oxide ( $ZnO$ ) (Gaya and Abdullah 2008).

In addition, a strategy to increase photocatalytic efficiency of photocatalysts is to modify their surface with metals (doping) (Ko et al. 2011; You et al. 2005), where these small metal particles facilitate the transfer of photoelectrons, promoting the reduction of the **band gap** energy, providing an application to visible radiation (Sakthivel et al. 2004). In parallel, materials synthesized using the **sol-gel route** have been widely studied due mainly to their structural and textural characteristics, such as high purity, porosity, specific area, and high homogeneity under low temperatures, being a

potential material for photocatalyst applications (Mardkhe et al. 2016).

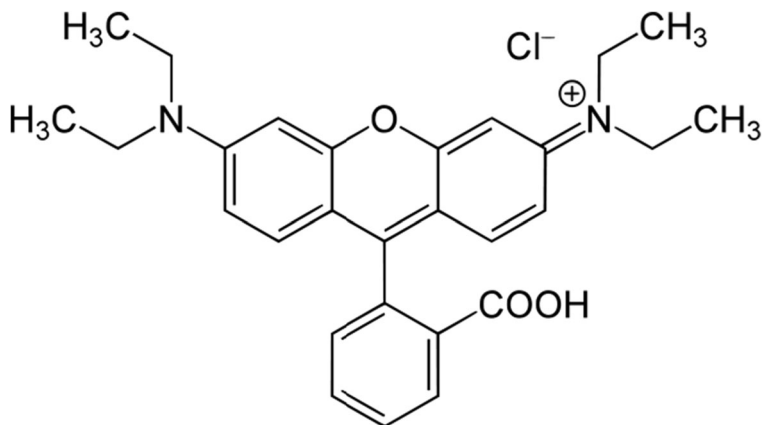
In this context, the present work aims to evaluate the potential of heterogeneous silica-based photocatalysts synthesized by sol-gel route, evaluating the effect of silver nanoparticle doping (AgNPs) on Rhodamine B (RhB) dye degradation, such as a target molecule under UV and visible radiation. Moreover, it also aims to correlate the photocatalytic activity with the elemental, structural, and textural properties of synthesized samples. For comparison, commercial titanium (Evonik Aeroxide P25) was used.

## 2 Methods

### 2.1 Materials

Tetraorthosilicate ( $Si(OC_2H_5)_4$ , Aldrich), nitric acid ( $HNO_3$ , Synth), ammonium hydroxide ( $NH_4OH$ , Neon), dodecylamine ( $C_{12}H_{27}N$ , Merck), and sodium hydroxide ( $NaOH$ , Neon) were used as precursor and catalysts, respectively. Ethanol ( $C_2H_5OH$ , Neon) and n-propanol ( $C_3H_8O$ , Vetec) were used to synthesize the silica-based materials. Rhodamine B ( $C_{28}H_{31}N_2O_3Cl$ , Synth) and titanium dioxide ( $TiO_2$ , Evonik) were used as the dye probe for the degradation tests and the commercial catalyst, respectively. Silver nitrate ( $AgNO_3$ , Synth) was used for the preparation of the doped photocatalysts. Double-distilled deionized water was used for the preparation of the solutions used in the catalytic tests.

**Fig. 1** Molecular structure of Rhodamine B dye (RhB)



## 2.2 Synthesis of the Photocatalysts by Sol-Gel Route

For the synthesis of the photocatalysts, the sol-gel route was used, according to the literature (Roucher et al. 2018), where four samples were synthesized with different compositions (solvent and catalyst), which were labeled with Si-X, where X refers to the different catalysts used during synthesis, according to Table 1.

The synthesis of the catalysts was performed by precursor hydrolysis and condensation (tetraorthosilicate) reactions, under constant magnetic stirring and at room temperature. Figure 2 shows the schematic representation of the steps during the sol-gel route.

## 2.3 Synthesis of Silver Nanoparticles

Silver nanoparticles (AgNPs) were synthesized according to the literature (Da Silva et al. 2016), where 75 mL of sodium borohydride solution ( $0.002 \text{ mol L}^{-1}$ , Neon, PA) was added, in ice bath, under magnetic stirring for 10–15 min with 25 mL of a silver nitrate solution ( $0.001 \text{ mol L}^{-1}$ , Synth, PA) (rate of  $1 \text{ drop s}^{-1}$ ), forming silver nanoparticles.

## 2.4 Synthesis of the Doped Catalyst

For doping of the synthesized catalyst (Si-X), the impregnation methodology with the respective photoactive metal precursor (AgNPs –  $\text{Ag}^+$ ) was used, according to the literature (Da Silva et al. 2016). Then, the catalyst (Si- $\text{HNO}_3$ ) was mixed with metal precursor ( $\text{AgNO}_3$ ) (25% w/w), under continuous magnetic stirring at room temperature for 90 min. Then, the sample was calcined ( $450 \text{ }^\circ\text{C}/240 \text{ min}$ ), uniformed its particle size through sieving (#12), labeled as Si- $\text{HNO}_3$ -AgNPs.

**Table 1** Nomenclature of heterogeneous catalysts synthesized by sol-gel route

Sample	Precursor	Solvent	Catalyst
Si- $\text{C}_{12}\text{H}_{27}\text{N}$	Tetraorthosilicate	Ethanol	Dodecylamine
Si- $\text{HNO}_3$	Tetraorthosilicate	n-Propanol	$\text{HNO}_3$
Si- $\text{NH}_4\text{OH}$	Tetraorthosilicate	n-Propanol	$\text{NH}_4\text{OH}$
Si- $\text{NaOH}$	Tetraorthosilicate	n-Propanol	$\text{NaOH}$

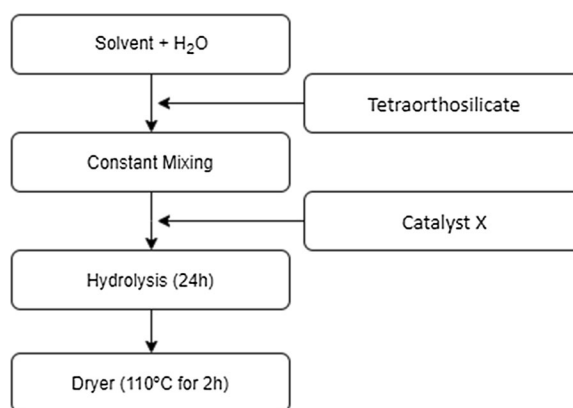


**Fig. 2** Schematic representation of the synthesis of the photocatalysts by sol-gel route

## 2.5 Characterization of the Photocatalysts

The X-ray diffraction technique was used to identify the crystalline phases in a copper tube X-ray diffractometer (Bruker Optics, D2 Advance, USA) ( $K\alpha$ -Cu radiation =  $1.5418 \text{ \AA}$ ), with an angular range ( $2\theta$ ) from  $5^\circ$  to  $70^\circ$ , acceleration voltage and applied current of 30 kV and 30 mA, respectively.

The Fourier transform infrared spectroscopy (FTIR) was used to obtain information about the functional groups using the Varian 640-IR Fourier Transform Spectroscopy Infrared (South Africa) in the region  $4000$  to  $500 \text{ cm}^{-1}$  with 32 scans and  $4 \text{ cm}^{-1}$  resolution (transmission mode).

The Malvern-Zetasizer® model nanoZS (ZEN3600, UK) with closed capillary cell (DTS 1060) (Malvern, UK) was used to measure the zeta potential (PZ) and to determine the surface charge.

Specific surface area, pore diameter, and pore volume were determined by  $\text{N}_2$  porosimetry (99.99% ultrapure grade, White Martins) on a Gemini 2375 Micromeritics equipment (Micromeritics Gemini VII 2375 Series, USA) at a temperature of  $-196 \text{ }^\circ\text{C}$ , where initially the samples were previously treated ( $10^{-2} \text{ mbar}$  at  $120 \text{ }^\circ\text{C}$ ) for 24 h. Specific area ( $S_{\text{BET}}$ ) was determined by the Brunauer-Emmett-Teller equation (BET method) in the range of  $P/P_0 = 0.05$  to  $0.35$  and the pore and diameter sizes were calculated using the Barrrt-Joyner-Halenda (BJH) equation.

The band gap energy was determined by diffuse reflectance spectroscopy (DRS) on a UV-visible spectrophotometer (Cary 100 Scan, UV-Vis Spectrophotometers, USA) with DRA-CA-301 accessory (Labsphere, USA) coupled for analysis in diffuse reflectance mode ( $200$ – $600 \text{ nm}$ ).

## 2.6 Photocatalytic Activity Tests

In photocatalytic tests, photocatalyst ( $0.7 \text{ g L}^{-1}$ ) was added in 50 mL of the solution containing the target molecule ( $20 \text{ mg L}^{-1}$ ). These tests were performed in two steps, according to the literature (Da Silva et al. 2016). The first (dark stage) was in the absence of radiation, where the adsorption/desorption equilibrium of the target molecule occurred over the catalyst surface (60 min). The second stage was a photocatalytic reaction with the presence of radiation (visible or UV) during 120 min.

Moreover, photodegradation was monitored using a syringe/catheter system (1 mL), where samples were collected at predetermined times (0, 5, 15, 30, 45, 60, 75, 90, and 120 min), centrifuged (Refrigerated Digital Bank Centrifuge, Cientec CT-5000R, Brazil) for 20 min with rotation of 5000 rpm, temperature of  $25 \text{ }^\circ\text{C}$ , and 1 min of acceleration/deceleration, and diluted (0.5 mL of sample in 5 mL of distilled water). To advance the reaction, the absorbance measurements of the solutions collected along the reaction were performed, at the characteristic wavelength of the RhB dye (553 nm).

All photocatalytic tests were performed in duplicate (with error less than 5%) and the radiation adjusted to  $202 \text{ W m}^{-2}$  for visible (Pyrometer, Type SL 100Skilltech Instruments, Brazil) and  $61.8 \text{ W m}^{-2}$  for ultraviolet (Radiometer Cole-Parmer Instrument, Radiometer Series 9811, USA).

## 2.7 Heterogeneous Kinetics

Experimental results indicate that the photocatalytic oxidation of contaminant degradation fits the Langmuir-Hinshelwood (L-H) kinetic model for unimolecular reactions (Konstantinou and Konstantinou and Albanis 2004). Then, the L-H model identifies three main steps of a heterogeneous reaction: reagent adsorption on the catalyst surface, surface reaction, and product desorption, being the slowest surface reaction step and responsible for the reaction kinetics, according to Eq. (1).

$$-r_i = -\frac{dC_i}{dt} = \frac{\kappa_S \cdot K \cdot C_i}{1 + K \cdot C_i} \quad (1)$$

where

$-r_i$	reaction rate
$\kappa_S$	specific speed of surface reaction
$C_i$	reagent concentration
	reagent adsorption constant on the catalyst surface

$K$

For systems where the reagent is sufficiently diluted, the term  $K C_i$  in the denominator of Eq. (1) is much less than 1 and may be disregarded. In this way, we get Eq. (2) which when integrated generates Eq. (3).

$$-r_i = -\frac{dC_i}{dt} = \kappa_S \cdot K \cdot C_i \quad (2)$$

$$\ln\left(\frac{C_{i0}}{C_i}\right) = \kappa_S \cdot K \cdot t = \kappa \cdot t \text{ or } C_i = C_{i0} \cdot e^{-\kappa t} \quad (3)$$

## 2.8 Statistical Analysis

Correlation data between photocatalytic activity and characterization results were obtained by Pearson's correlation method using SPSS statistical software (SPSS for Windows, version 19, IBM®). All statistical tests were performed at the significance level of  $p < 0.05$ , where Pearson's correlation coefficient ( $r_p$ ) was used as a measure of nonparametric statistical dependence between two variables, indicating positive or negative correlations.

## 3 Results and Discussion

### 3.1 Characterization of the Photocatalysts

#### 3.1.1 Zeta Potential

Zeta potential (ZP) measurements were used to verify the stability of particle suspensions of the photocatalysts, as well as their surface charge, to verify the influence of RhB adsorption on the samples. For example, if the dye to be degraded and the semiconductor have opposite charges, there is a greater electrostatic attraction and the possibility of adsorption interaction becomes favorable, affecting photocatalytic activity (Ko et al. 2011). Table 2 shows the respective zeta potential (ZP) results, while Fig. 3 shows the zeta potential curves of the synthesized and doped samples. For comparison, the ZP value of the commercial catalyst ( $\text{TiO}_2$ ) was also determined.

According to Table 2 and Fig. 3, all samples showed negative surface charge in the range of  $-17.7$  to  $-48.1 \text{ mV}$ , indicating a charge compatibility between the surface potential and the charge of the molecule to be degraded (RhB), becoming favorable the adsorption. In addition, the RhB molecule is characterized by a

**Table 2** Zeta potential of samples

Samples	ZP (mV)
Si-C <sub>12</sub> H <sub>27</sub> N	-32.7 ± 0.737
Si-HNO <sub>3</sub>	-24.8 ± 0.306
Si-NH <sub>4</sub> OH	-37.4 ± 0.624
Si-NaOH	-48.1 ± 0.20
Si-HNO <sub>3</sub> -AgNPs	-17.7 ± 0.971
TiO <sub>2</sub> (P25)	-24.0 ± 0.50

positive charge due to its cationic nature (Salleh et al. 2011) and the synthesized photocatalysts are negatively charged, so the RhB dye tends to adsorb onto the catalytic surface of the photocatalysts by means of attractive forces, thus allowing the degradation of the pollutant.

### 3.1.2 X-ray Diffraction

The characterization of the crystalline structure was determined using X-ray diffraction (XRD) analysis, indicating that the samples have an amorphous structure, characteristic of materials derived from silica, as shown in Fig. 4.

According to Fig. 4, 2 $\theta$  amorphous peak is equal to 22.5°, representing the amorphous SiO<sub>2</sub> phase since the process did not favor the crystallization of silica (Roucher et al. 2018). Moreover, the doped sample has a displacement relative to the other samples, since the silver nanoparticles are deposited on the material surface. The presence of the broad peak is characteristic of nanometric

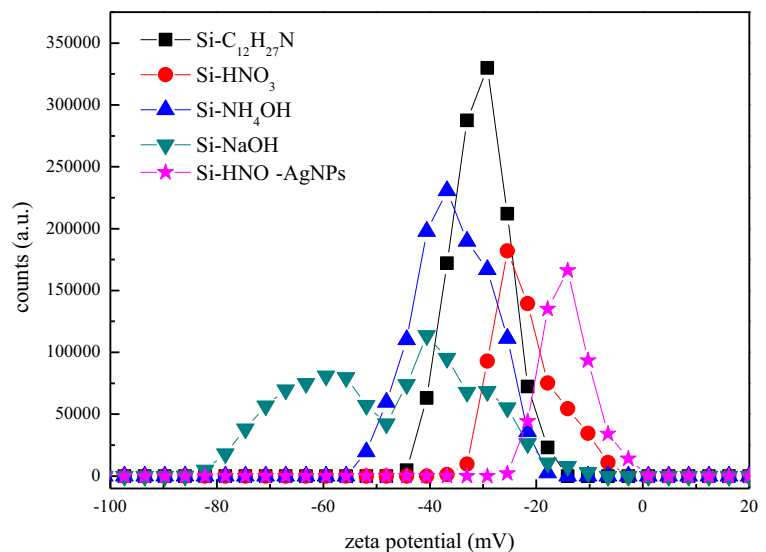
particles (Shameli et al. 2011), thus justifying the subtle displacement with the amorphous peak of silica.

### 3.1.3 Fourier Transform Infrared Spectroscopy

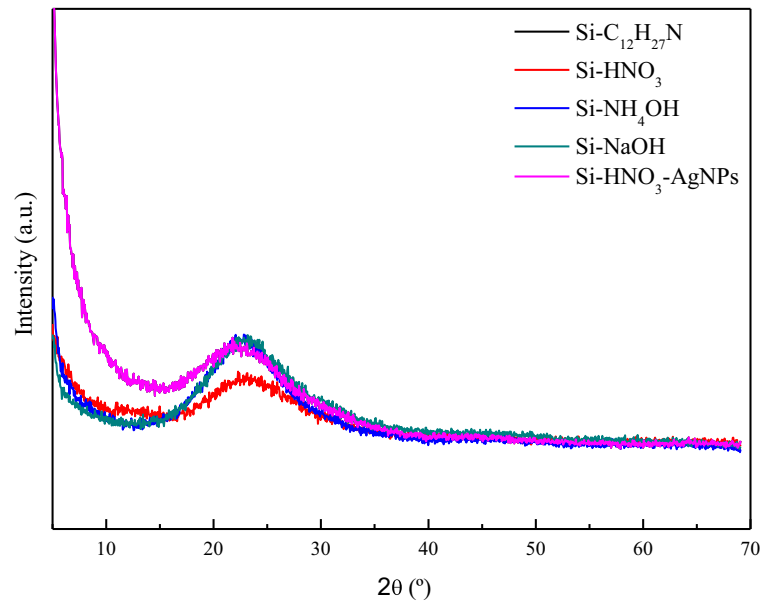
Figure 5 a shows the infrared vibrational spectra of the synthesized samples, while Fig. 5b the doped sample spectrum (Si-HNO<sub>3</sub>-AgNPs), where some common characteristic peaks are possible, such as (Benvenuti et al. 2009) (1) a broad and wide bank between 3600 and 3400 cm<sup>-1</sup> attributed to the -OH stretching frequency of the precursor agent (tetraorthosilicate) silanol groups and also the remaining adsorbed water; (2) in the region of 1635 cm<sup>-1</sup>, a peak corresponding to the angular deformation of the water molecule (-HO-H); (3) an intense band with respect to the asymmetric stretch of siloxane attributed to the Si-O-Si vibrations at 1140 and 1050 cm<sup>-1</sup>; (4) the peak corresponding to the deformation frequency of the Si-O-H group at 915 cm<sup>-1</sup>; and (5) a peak at 480 cm<sup>-1</sup> assigned to the -O-Si-O bond. Thus, these characteristic peaks confirm the hydrolysis reactions and formation of silica-based material. While for the doped sample (Fig. 5b), the functional groups remained, guaranteeing the condensation and hydrolysis reactions of the synthesis.

### 3.1.4 Nitrogen Porosimetry

The surface area ( $S_{BET}$ ), pore diameter ( $D_p$ ), and pore volume ( $V_p$ ) of the synthesized and doped samples were obtained using the BET/BJH methods and are illustrated

**Fig. 3** Zeta potential curves of photocatalysts

**Fig. 4** XRD diffractograms of the samples



in Table 3. In addition, the  $N_2$  adsorption/desorption isotherms of synthesized and doped samples are shown in Fig. 6. For comparative purposes, commercial P25 catalyst ( $TiO_2$ ) was also included.

According to Table 3 and Fig. 6, the doped sample ( $Si-HNO_3-AgNPs$ ) presented higher  $S_{BET}$  value ( $614.51 \text{ m}^2 \text{ g}^{-1}$ ) and larger pore volume ( $0.603 \text{ cm}^3 \text{ g}^{-1}$ ). In addition,  $Ag^+$  doping promoted changes in textural properties compared with the undoped sample ( $Si-HNO_3$ ), such as an increase from  $389.56$  to  $614.51 \text{ m}^2 \text{ g}^{-1}$  in the specific area and  $0.214$  to  $0.603 \text{ cm}^3 \text{ g}^{-1}$  in pore volume. It is noteworthy that for heterogeneous photocatalysis, the ideal is that the photocatalyst has a high specific area to promote more adsorption of the pollutant to be degraded, as well as a significantly large pore volume to promote the pollutant diffusion to the catalytic surface of the photocatalyst (Wang et al. 2008). Moreover, through pore diameter, it is possible to state that they are structures with mesoporous (Everett 1972) with isotherms type IV with hysteresis type H1 ( $Si-NH_4OH$ ) and H2 ( $Si-C_{12}H_{27}N$ ,  $Si-HNO_3$ ,  $Si-NaOH$ , and  $Si-HNO_3-AgNPs$ ) characteristics of mesoporous structures where type H1 is a relatively uniform pore distribution, while type H2 is associated with a more complex structure in which the pore size and shape are not well defined.

### 3.1.5 Diffuse Reflectance Spectroscopy

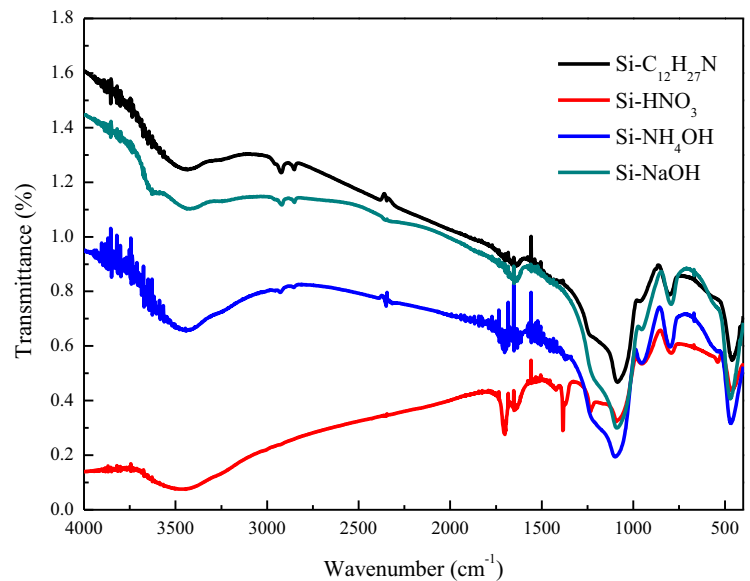
The forbidden band or band gap energy ( $E_g$ ) was determined by diffuse reflectance spectroscopy, emphasizing that it is an extremely relevant parameter for the photocatalytic process, since the lower the  $E_g$ , the lower the radiation energy required for the photocatalytic process activation, making it applicable to the visible light region.

Thus, to determine the photoabsorbance properties, DRS analyses were performed in the wavelength range of  $200-600 \text{ nm}$ , where a straight line is a projected tangent to the slope of the curve, obtaining the characteristic wavelength and through Eq. (1) calculates the band gap energy. Thus, Table 4 presents the results obtained from the band gap energy of the synthesized samples and, for comparison, data from the commercial P25 catalyst ( $TiO_2$ ) were included.

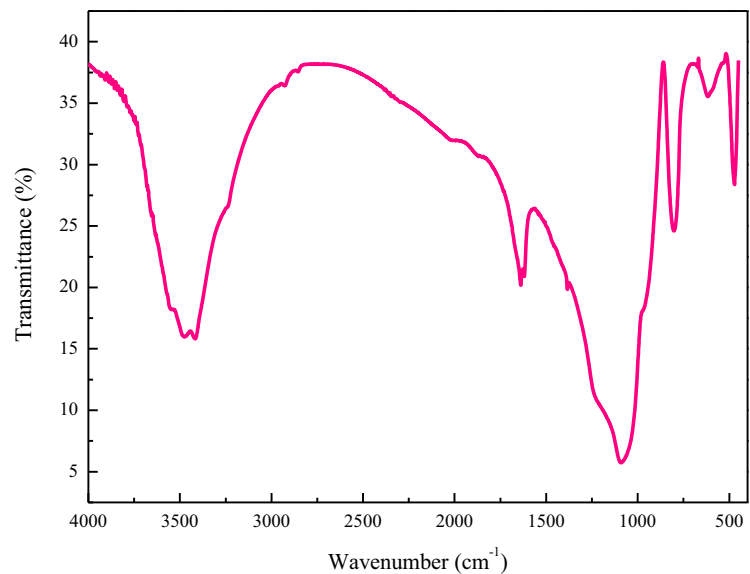
According to Table 4, the obtained band gap values ranged from  $2.52$  to  $5.6 \text{ eV}$ . Moreover, it can be observed that the sample doped with silver nanoparticles ( $Si-HNO_3-AgNO_3$ ) presented the lowest  $E_g$  value ( $2.52 \text{ eV}$ ) and, among the different catalysts used for sol-gel synthesis, undoped sample using  $HNO_3$  presented lower  $E_g$  ( $2.72 \text{ eV}$ ). It is important that the samples  $Si-C_{12}H_{27}N$ ,  $Si-HNO_3$ ,  $Si-NH_4OH$ , and  $Si-HNO_3-AgNPs$  presented their respective wavelengths within the visible region adsorption range ( $400-750 \text{ nm}$ ), indicating a possible application under visible and solar



**Fig. 5** FTIR spectrum of synthesis (a) and doped (b)



(a)



(b)

radiation, as well as lower  $E_g$  values than the commercial catalyst ( $\text{TiO}_2$  P25). Furthermore, it was possible to verify that doping with silver nanoparticles promoted a reduction on  $E_g$ , causing a shift towards light absorption in the visible range and thus directly affecting photocatalytic activity. This was possibly because, with silver doping

( $\text{Ag}^+$ ), the concentration of electron-acceptor/donor species ( $e_{\text{BC}}^-$  and  $h_{\text{BV}}^+$ ) increases, followed by a decrease in  $\text{O}^{2-}$  ion polarization in the conduction band. Thus, it promotes a change in the conduction bands and valence band levels, promoting a reduction in the photocatalysts energy band interval (Da Silva et al. 2016).

**Table 3** Surface area, pore diameter and pore volume of samples

Samples	$S_{\text{BET}}$ ( $\text{m}^2 \text{g}^{-1}$ )	Dp (nm)	Vp ( $\text{cm}^3 \text{g}^{-1}$ )
Si-C <sub>12</sub> H <sub>27</sub> N	297.73	2.71	0.235
Si-HNO <sub>3</sub>	389.56	2.49	0.214
Si-NH <sub>4</sub> OH	376.99	4.39	0.497
Si-NaOH	1.85	14.69	0.0074
Si-HNO <sub>3</sub> -AgNPs	614.51	3.54	0.603
TiO <sub>2</sub> (P25)	56	4.8	0.07

**Table 4** Photon energies applied by UV-visible absorption spectra with wave components

Samples	$\lambda$ (nm)	Eg (eV)
Si-C <sub>12</sub> H <sub>27</sub> N	411.96	3.01
Si-HNO <sub>3</sub>	455.88	2.72
Si-NH <sub>4</sub> OH	441.28	2.81
Si-NaOH	221.43	5.6
Si-HNO <sub>3</sub> -AgNPs	492.06	2.52
TiO <sub>2</sub> (P25)	371.25	3.34

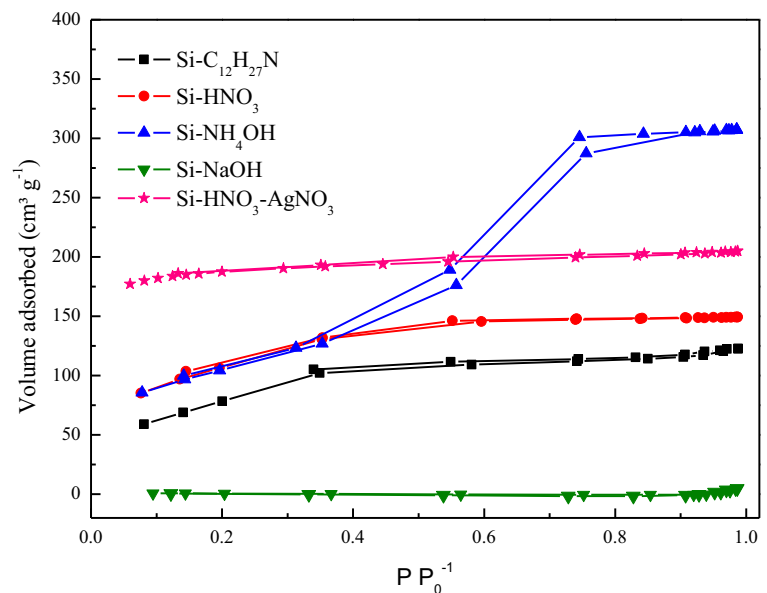
### 3.2 Photocatalytic Activity

The photocatalytic activity of samples synthesized via sol-gel route and doped route (Si-HNO<sub>3</sub>-AgNPs) was evaluated by RhB dye degradation ( $20 \text{ mg L}^{-1}$ ), under UV and visible radiation and concentration of  $0.7 \text{ g L}^{-1}$ , according to predetermined methodology (Da Silva et al. 2016). Thus, Fig. 7 shows the photocatalytic degradation activity of RhB and the respective specific reaction rates ( $k$ ) under ultraviolet radiation, while Fig. 8 shows the visible range after 120 min of reaction.

Under ultraviolet radiation (Fig. 7), Si-HNO<sub>3</sub>-AgNPs sample presented the highest degradation (90.16% and  $k = 0.0198 \text{ min}^{-1}$ ), a fact that can be justified by its textural and structural characteristics, as larger area ( $S_{\text{BET}}$ ) and pore volume (Vp), lower band gap energy (Eg), and negative surface charge, providing better mass transfer and diffusion of RhB molecules

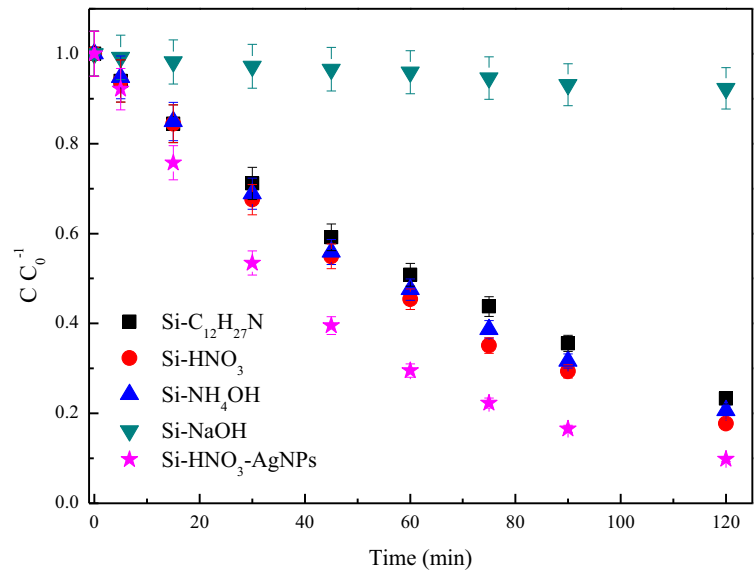
and thus better photocatalytic activity. Regarding the commercial catalyst (TiO<sub>2</sub> P25), Si-HNO<sub>3</sub>-AgNPs, Si-HNO<sub>3</sub>, Si-NH<sub>4</sub>OH, and Si-C<sub>12</sub>H<sub>27</sub>N samples had a better catalytic performance under UV radiation, while TiO<sub>2</sub> showed a degradation of 50.02% ( $k = 0.0057 \text{ min}^{-1}$ ) after 120 min of reaction; undoped samples showed 82.29% ( $k = 0.0139 \text{ min}^{-1}$ ), 79.34% ( $k = 0.0125 \text{ min}^{-1}$ ), and 76.72% ( $k = 0.0117 \text{ min}^{-1}$ ) for Si-HNO<sub>3</sub>, Si-NH<sub>4</sub>OH, Si-C<sub>12</sub>H<sub>27</sub>N, and Si-NaOH samples, respectively, under the same conditions.

While under visible radiation (Fig. 8), the Si-HNO<sub>3</sub>-AgNPs sample (82.79% and  $k = 0.0148 \text{ min}^{-1}$ ) showed an increase of about 14.26% in its photocatalytic activity after doping with the silver nanoparticles, compared with the Si-HNO<sub>3</sub> sample (72.46% and  $k = 0.0105 \text{ min}^{-1}$ ), presenting the highest photocatalytic activity, as well as in ultraviolet radiation. In all

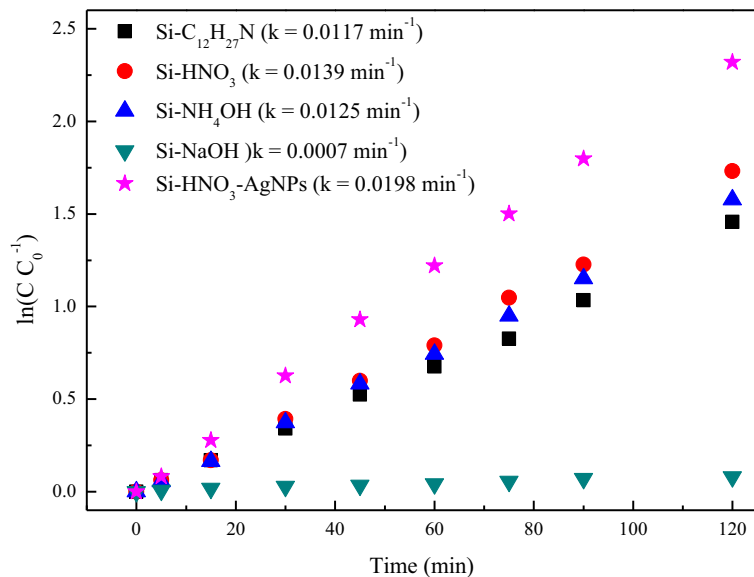
**Fig. 6** Isotherm of adsorption/desorption of N<sub>2</sub> for samples synthesized and doped with Ag<sup>+</sup>



**Fig. 7** **a** Photocatalytic activity and **b** specific speed of RhB dye degradation reaction of synthesized and doped samples under UV radiation after 120 min of reaction ( $C_{\text{cat}} = 0.7 \text{ g L}^{-1}$ ,  $C_{\text{RhB}} = 20 \text{ mg L}^{-1}$ ,  $T = 30 \text{ }^\circ\text{C}$ , natural pH and radiation intensity UV of  $61.8 \text{ W m}^{-2}$ )



(a)



(b)

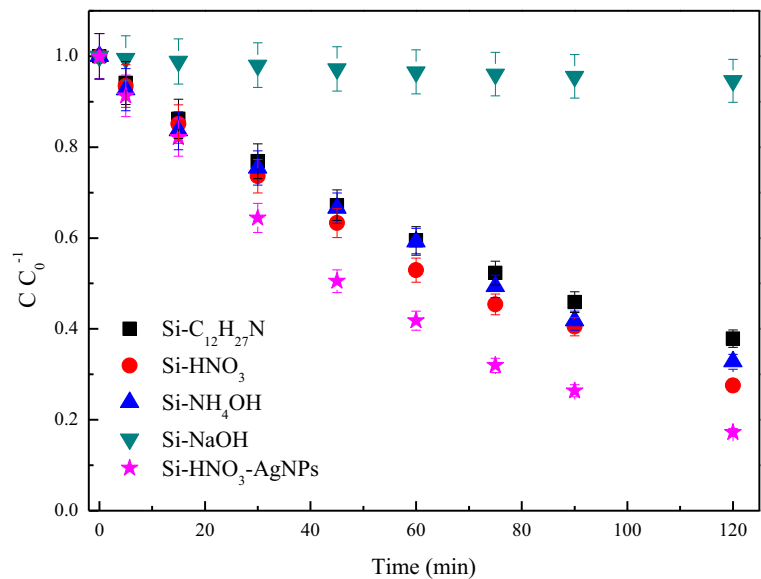
degradation processes, the reactions followed a pseudo first-order kinetics. Regarding the commercial catalyst ( $\text{TiO}_2$  P25),  $\text{Si-HNO}_3\text{-AgNPs}$ ,  $\text{Si-HNO}_3$ ,  $\text{Si-NH}_4\text{OH}$ , and  $\text{Si-C}_{12}\text{H}_{27}\text{N}$  samples had a better catalytic performance under visible radiation, i.e., while  $\text{TiO}_2$  showed a degradation of 42.14% ( $k = 0.0043 \text{ min}^{-1}$ ) after 120 min of reaction, undoped samples showed 72.46% ( $k = 0.0105 \text{ min}^{-1}$ ), 67.21% ( $k = 0.0094 \text{ min}^{-1}$ ), and 62.13% ( $k = 0.0084 \text{ min}^{-1}$ ) for  $\text{Si-HNO}_3$ ,  $\text{Si-NH}_4\text{OH}$ ,

$\text{Si-C}_{12}\text{H}_{27}\text{N}$ , and  $\text{Si-NaOH}$  samples, respectively under the same conditions.

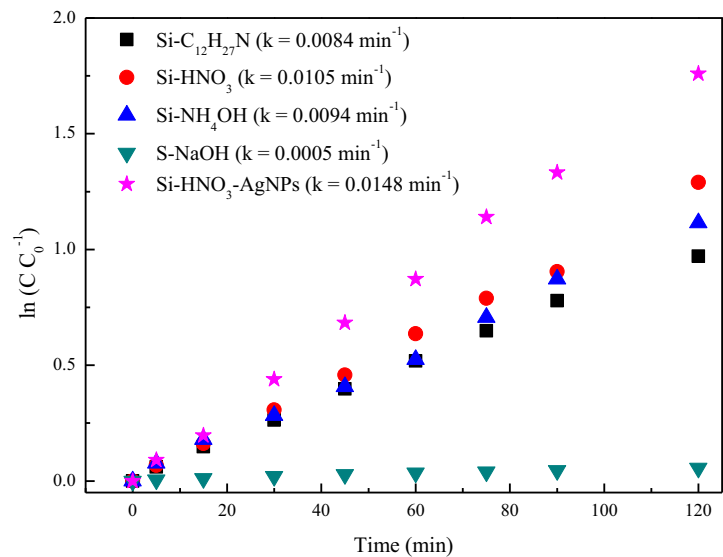
Table 5 features the respective values of the specific reaction rate ( $k$ ) and the respective degradations.

Some of Pearson's main correlations were observed, using the SPSS statistical software, between the characterization results and the specific reaction variations, as shown in Fig. 9. It is noteworthy that a direct or indirect correlation is the same as a correlation coefficient

**Fig. 8** **a** Photocatalytic activity and **b** specific speed of RhB dye degradation reaction of synthesized and doped samples under UV radiation after 120 min of reaction ( $C_{\text{cat}} = 0.7 \text{ g L}^{-1}$ ,  $C_{\text{RhB}} = 20 \text{ mg L}^{-1}$ ,  $T = 30 \text{ }^\circ\text{C}$ , natural pH and visible radiation intensity of  $202 \text{ W m}^{-2}$ )



(a)



(b)

greater than 0.70 or greater than 70% of the variation of one of the variables is explained by the other variable.

Figure 9 a shows a direct correlation between surface area and respective specific velocities under UV ( $rp = 0.993$ ) and visible ( $rp = 0.995$ ) radiation, indicating that for a larger specific surface area, the higher the specific velocities of the surface area and reaction and, consequently, greater photocatalytic activity, since

more active sites are available, thus greater RhB adsorption and a higher generation of hydroxyl radicals (Vadivel and Rajarajan 2015). Meanwhile, Fig. 9b shows an indirect correlation of band gap energy ( $E_g$ ) ( $rp = -0.938$  and  $rp = -0.936$  under UV and visible radiation, respectively) with photocatalytic activity. Thus, for lower  $E_g$  values, higher reaction specific velocity values, photocatalysts are more easily

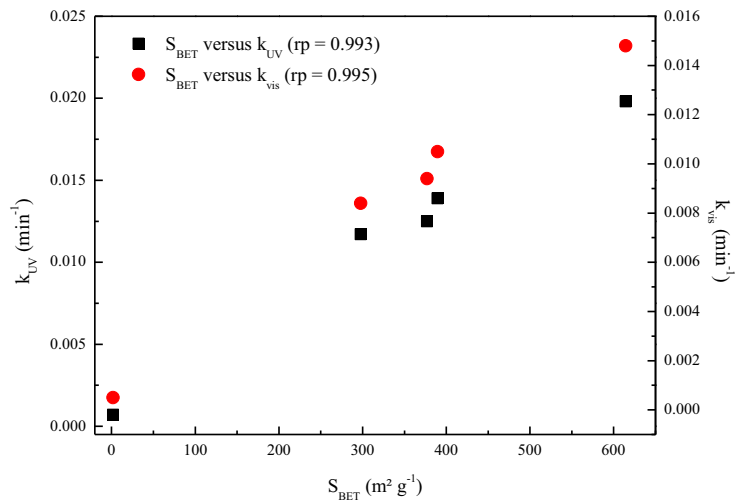
**Table 5** Specific reaction speeds (*k*) under UV and visible radiation

Catalyst	% degradation (UV)	$k_{UV}$ (min <sup>-1</sup> )	% degradation (vis)	$k_{vis}$ (min <sup>-1</sup> )
Si-C <sub>12</sub> H <sub>27</sub> N	76.72	0.0117	62.13	0.0084
Si-HNO <sub>3</sub>	82.29	0.0139	72.46	0.0105
Si-NH <sub>4</sub> OH	79.34	0.0125	67.21	0.0094
Si-NaOH	7.70	0.0007	5.41	0.0005
Si-HNO <sub>3</sub> -AgNPs	90.16	0.0198	82.79	0.0148
TiO <sub>2</sub> (P25)	50.02	0.0057	42.14	0.0043

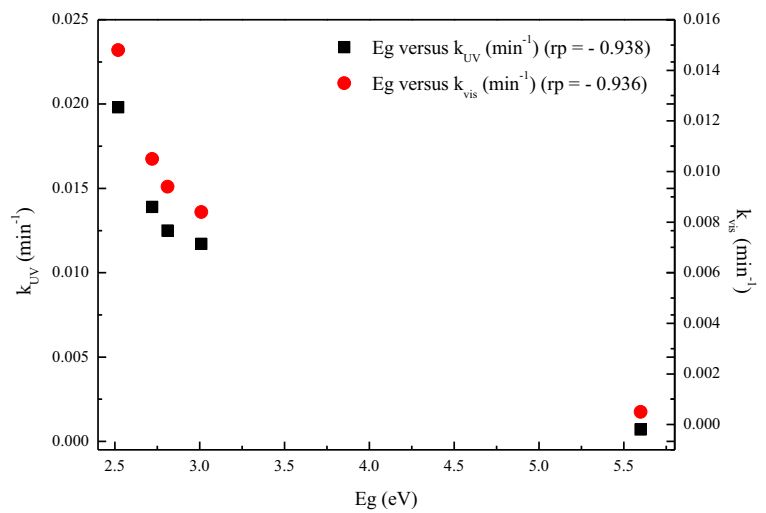
activated, facilitating oxi-reduction reactions for degradation of organic pollutants providing greater

photocatalytic activity in the target molecule degradation under UV and visible radiation.

**Fig. 9** Correlations between specific reaction rates of RhB degradation under UV and visible radiation with **a** surface area ( $S_{BET}$ ) and **b** band gap energy ( $E_g$ )



(a)



(b)

## 4 Conclusion

Based on the results presented, it can be concluded that the photodegradation kinetics of the Rhodamine B dye can be approximated for a pseudo first-order model and that silver nanoparticle ( $\text{Ag}^+$ ) doping provided changes in textural and structural properties, in some cases compared with undoped samples, such as reduction in band gap energy ( $E_g$ ), increase in surface area ( $S_{\text{BET}}$ ), and pore volume ( $V_p$ ) and a better photocatalytic performance in RhB dye degradation on UV and visible radiation. Thus, these results suggest that the positive effect of silver as a dopant on the development of silica-based photocatalysts, because  $\text{Ag}^+$  is capable of generating an intermediate band gap energy between the conduction and valence bands of the sample doped, is capable of promoting photon absorption and generating more electron/holes pairs ( $e_{\text{BC}}^-$  and  $h_{\text{BV}}^+$ ) and thus providing greater hydroxyl radical ( $\bullet\text{OH}$ ) formation. Therefore, photocatalysts synthesized via sol-gel route and doped with silver nanoparticles are promising for use in the degradation of organic pollutants by heterogeneous photocatalysis.

**Acknowledgments** We thank the Catalysis and Polymers Laboratory (K106) of the Federal University of Rio Grande do Sul (UFRGS) for their support and assistance in carrying out this work.

**Funding Information** This work received financial support from the Foundation for Research of the State of Rio Grande do Sul (FAPERGS – Project 19/2551-0001362-0).

## References

- Al-Fawwaz, A. T., & Abdullah, M. (2015). Decolorization of methylene blue and malachite green by immobilized *Desmodesmus* sp. isolated from North Jordan. *International Journal of Environmental Science and Development*, 7(2), 95–99.
- Benvenuti, E. V., Moro, C. C., Costa, T. M. H., & Gallas, M. R. (2009). Silica based hybrid materials obtained by the sol-gel method. *Química Nova*, 32(7), 1926–1933.
- Cheng, Z., Li, Y., & Liu, Z. (2017). Fabrication of graphene oxide/silicalite-1 composites with hierarchical porous structure and investigation on their adsorption performance for rhodamine B. *Journal of Industrial and Engineering Chemistry*, 55(1), 234–243.
- Da Silva, W. L., Lansarin, M. A., Dos Santos, J. H. Z., & Silveira, F. (2016). Photocatalytic degradation of rhodamine B, paracetamol and diclofenac sodium by supported titania-based catalysts from petrochemical residue: effect of doping with magnesium. *Water Science and Technology*, 74(10), 2370–2383.
- Everett, D. H. (1972). Manual of symbols and terminology for physicochemical quantities and units, appendix II: definitions, terminology and symbols in colloid and surface chemistry. *Pure and Applied Chemistry*, 31(4), 578–638.
- Gao, Y., Wang, Y., & Zhang, H. (2015). Removal of Rhodamine B with Fe-supported bentonite as heterogeneous photo-Fenton catalyst under visible irradiation. *Applied Catalysis B: Environmental*, 178(1), 29–36.
- Gaya, U. I., & Abdullah, A. H. (2008). Heterogeneous photocatalytic degradation of organic contaminants over titanium dioxide: a review of fundamentals, progress and problems. *Journal of Photochemistry and Photobiology C: Photochemistry Reviews*, 9(1), 1–12.
- Kassale, A., Barouni, K., Martins, J. I., & Albourine, A. (2015). Methylene blue adsorption by cotton grafted with succinic anhydride. *Protection of Metals and Physical Chemistry of Surfaces*, 51(3), 382–389.
- Ko, S., Banerjee, C. K., & Sankar, J. (2011). Photochemical synthesis and photocatalytic activity in simulated solar light of nanosized Ag doped  $\text{TiO}_2$  nanoparticle composite. *Composites Part B: Engineering*, 42(3), 579–583.
- Konstantinou, I. K., & Albanis, T. A. (2004). Photocatalytic transformation of pesticides in aqueous titanium dioxide suspensions using artificial and solar light: intermediates and degradation pathways. *Applied Catalysis B: Environmental*, 42(4), 319–335.
- Lu, H., Li, H., Wang, Y., & Li, X. (2019). Preparation of  $\text{CoFe}_2\text{O}_4@vacancy@m\text{SiO}_2$  core-shell composites for removal of organic pollutant in aqueous solution. *Journal of Saudi Chemical Society*, 23(5), 536–545.
- Ma, J., Li, L., Zou, J., Kong, Y., & Komameni, S. (2014). Highly efficient visible light degradation of Rhodamine B by nanophase  $\text{Ag}_3\text{PO}_4$  dispersed on SBA-15. *Microporous and Mesoporous Materials*, 193(1), 154–159.
- Mardkhe, M. K., Huang, B., Bartholomew, C. H., Alam, T. M., & Woodfield, B. F. (2016). Synthesis and characterization of silica doped alumina catalyst support with superior thermal stability and unique pore properties. *Journal of Porous Materials*, 23(2), 475–487.
- Patil, S. P., Bethi, B., Sonawane, G. H., Shrivastava, V. S., & Sonawane, S. (2016). Efficient adsorption and photocatalytic degradation of Rhodamine B dye over  $\text{Bi}_2\text{O}_3$ -bentonite nanocomposites: a kinetic study. *Journal of Industrial and Engineering Chemistry*, 34(1), 356–363.
- Rafatullah, M., Sulaiman, O., Hashim, R., & Ahmad, A. (2010). Adsorption of methylene blue on low-cost adsorbents: a review. *Journal of Hazardous Materials*, 177(1–3), 70–80.
- Rajkumar, D., & Kim, J. G. (2006). Oxidation of various reactive dyes with in situ electro-generated active chlorine for textile dyeing industry wastewater treatment. *Journal of Hazardous Materials*, 136(2), 203–212.
- Roucher, A., Bentaleb, A., Laurichesse, E., Dourges, M., Emo, M., Schmitt, V., Blin, J., & Backov, R. (2018). First macrosocellular silica SBA-15-Si(HIPE) Monoliths: conditions for obtaining self-standing materials. *Chemistry of Materials*, 30(3), 864–873.
- Sakthivel, S., Shankar, M. V., Palanichamy, M., Arabindoo, B., Bahnemann, D. W., & Murugesan, V. (2004). Enhancement of photocatalytic activity by metal deposition:

- characterization and photonic efficiency of Pt, Au and Pd deposited on TiO<sub>2</sub> catalyst. *Water Research*, 38(13), 3001–3008.
- Salleh, M. A. M., Mahmoud, D. K., Karim, W. A. W. A., & Idris, A. (2011). Cationic and anionic dye adsorption by agricultural solid wastes: a comprehensive review. *Desalination*, 280(1–3), 1–13.
- Shameli, K., Ahmad, M. B., Zargar, M., Yunus, W. M. Z. W., Rustaiyan, A., & Ibrahim, N. A. (2011). Synthesis of silver nanoparticles in montmorillonite and their antibacterial behavior. *International Journal of Nanomedicine*, 6(1), 581–590.
- Vadivel, S., & Rajarajan, C. (2015). Effect of Mg doping on structural, optical and photocatalytic activity of SnO<sub>2</sub> nanostructure thin films. *Journal of Materials Science: Materials in Electronics*, 26(5), 3155–3162.
- Wang, M., Song, G., Li, J., Miao, L., & Zhang, B. (2008). Direct hydrothermal synthesis and magnetic property of titanate nanotubes doped magnetic metal ions. *Journal of University of Science and Technology Beijing, Mineral, Metallurgy, Material*, 15(5), 644–648.
- Wu, Q., Zhang, H., Zhou, L., Bao, C., Zhu, H., & Zhang, Y. (2016). Synthesis and application of rGO/CoFe<sub>2</sub>O<sub>4</sub> composite for catalytic degradation of methylene blue on heterogeneous Fenton-like oxidation. *Journal of the Taiwan Institute of Chemical Engineers*, 67(1), 484–494.
- You, X., Chen, F., Zhang, J., & Anpo, M. (2005). A novel deposition precipitation method for preparation of Ag-loaded titanium dioxide. *Catalysis Letters*, 102(3–4), 247–250.
- Zhang, J., Gondal, M. A., Wei, W., Zhang, T., Xu, Q., & Shen, K. (2012). Preparation of room temperature ferromagnetic BiFeO<sub>3</sub> and its application as a highly efficient magnetic separable adsorbent for removal of Rhodamine B from aqueous solution. *Journal of Alloys and Compounds*, 530(1), 107–110.

**Publisher's Note** Springer Nature remains neutral with regard to jurisdictional claims in published maps and institutional affiliations.